Electronic Supplementary Information

Dispersions of magnetic nanoparticles in dense ionic fluids - Influence of water and of the solid/liquid interface on the colloidal and transport properties

Ana Alice A. M. Guerra, Thiago Fiuza, Guilherme Gomide, Cynara Kern, Barbara C.C. Pereira, Mitradeep Sarkar, Nour Reguigui, Renata Aquino, Alex F.C. Campos, Priscilla Coppola, Gilles Demouchy, Jérôme Depeyrot, Emmanuelle Dubois, Régine Perzynski, Véronique Peyre

---

S1. Chemical Synthesis and Sample Preparation

S1.1. Materials and process for the synthesis of the NPs dispersed in acidic aqueous medium.

The following materials were used without further purification for the synthesis of maghemite NPs: nitric acid (69.5 % water solution, Carlo Erba); Sodium hydroxide (NaOH pellets, 98 %, Acros Organics); hydrochloric acid (HCl, 37 % water solution, AnalaR Normapur); iron(II) chloride ($FeCl_2$*$4H_2O$, AnalaR Normapur, VWR); iron(III) chloride ($FeCl_3$*$6H_2O$, Prolabo); iron(III) nitrate ($Fe(NO_3)_3$*$9H_2O$, technical, VWR); In addition, for the synthesis of the core@shell NPs, ammonium hydroxide (NH_4OH, solution 28-30% in water) and methylamine (CH_3NH_2, solution 40% in water) from Sigma-Aldrich are used. For samples C1, C2, C3, $FeCl_3$ and $Co(NO_3)_2$ from Vetec, Brasil, Analytical grade are used for the cores, and $Fe(NO_3)_3$ for their shell. For samples D, E and F, $FeCl_3$, $CoCl_2$, $CuCl_2$ and $ZnCl_2$ are used for the cores and $Fe(NO_3)_3$ for their shell, all from Aldrich, Analytical grade.

- Maghemite NPs are obtained in water, following the Massart's method [1, 2] by coprecipitation of acidic solutions of $FeCl_2$ and $FeCl_3$ with ammonium hydroxide as alkaline medium, then oxidized into maghemite (γ-Fe_2O_3) by a nitrate treatment at 100°C with a $Fe(NO_3)_3$ solution. At the end of the process the NPs are dispersed in water with protonated hydroxyl surface groups and nitrate counterions at $pH \sim 2$. These nanoparticles remain stable for years (even at least 15 years for some of the present samples) despite the low pH of the medium. This long-term stability is specific to nitric acid; in contrast, the use of hydrochloric acid (HCl) leads to particle dissolution within minutes or days, depending on the pH level. Their surface charge is then positive [3] with a superficial density of structural charge of the order of 2 elementary charges per nm^2 and with a point of zero charge (*PZC*) at $pH \sim 7$. It is possible to proceed to a size-sorting of the polydisperse NPs using their size-dependent colloid phase diagram as described in [4, 5] (see section S.1.3.). A and B NPs from Table 1 of main text are obtained in this way.

- Core@shell $CoFe_2O_4$@γ-Fe_2O_3 NPs are similarly obtained in water in a three-step procedure [6, 7]. First, the cobalt ferrite core is synthesized by coprecipitation of $CoCl_2$ and $FeCl_3$ in an alkaline medium at 100 °C under vigorous stirring, roughly tuning the NPs diameter through the strength of the base used in this step. As a general trend, the stronger the base, the larger the mean size, while keeping the other synthesis parameters constant [8]. At the second step, the maghemite shell is produced through a hydrothermal treatment with a $Fe(NO_3)_3$ solution. During this second step, a small leak of the under-coordinated surface divalent metal of the NP core is frequently observed [7, 9], as the iron-rich external layer settles. In the third step, the NPs are peptized in water at $pH \sim 2$, where they bear a positive structural surface charge [10] of approximately 2 charges per nm^2. Generally speaking, the surface properties of these NPs are qualitatively comparable to those of pure maghemite NPs and similar methods are used to produce NPs dispersions with a different coating, different counterions, at different *pH* in water or in different media [11].

Here the strength of the base employed in step 1 is used to produce NPs with different mean size. D1, D2 and D3 NPs are respectively obtained using ammonium hydroxide, methylamine and sodium hydroxide, leading to increasing

NP mean diameter. Another aqueous dispersion of NPs obtained using sodium hydroxide leading to the largest NPs, has been submitted to a subsequent size-sorting process of its polydisperse NP distribution, as described in [4] (see section S1.3 and Fig. S1) leading to the aqueous dispersions of C1, C2 and C3 NPs.

- ***Core@shell*** $\boldsymbol{Cu_{0.15}Zn_{0.15}Co_{0.7}Fe_2O_4@\gamma\text{-}Fe_2O_3}$ ***NPs*** are obtained following a process detailed in [12]. To obtain E NPs, the difference with the previous synthesis of $CoFe_2O_4@\gamma\text{-}Fe_2O_3$ NPs is at step 1 to obtain a stoichiometric mixed ferrite core $Cu_{0.15}Zn_{0.15}Co_{0.7}Fe_2O_4$. The hydrothermal coprecipitation is performed with a mixture of aqueous solutions of Fe^{3+}, Cu^{2+}, Zn^{2+} and Co^{2+}, in adapted proportions, in NaOH at 100 °C under vigorous stirring. The proportions of Cu, Zn, Co and Fe are determined by Energy Dissipative X-ray Spectroscopy (EDS) and Inductively Coupled Plasma (ICP) measurements in [12].

The iron-rich surface layer of core@shell NPs depends on the duration of the surface treatment, on the nature of the underlying core and on the mean NP diameter [7, 9, 13]. Its density is close to that of maghemite [7]. XRD measurements on such core@shell NPs only detect one spinel structure corresponding to the core and the shell altogether [7, 9, 13]. Coupled X-ray X-ray Absorption Spectroscopy (XANES/EXAFS) and Diffraction Anomalous Fine Structure (DAFS) on $CoFe_2O_4@\gamma\text{-}Fe_2O_3$ NPs [9] have shown that the hydrothermal surface treatment does not change the cations distribution of the NP core and that the iron oxide shell contains under-coordinated surface iron atoms with iron vacancies in B sites. The shell can be visualized when it is large enough by High Resolution Transmission Electron Microscopy (HRTEM) and Scanning Transmission Electron Microscopy (STEM) [14] or detected by EDS [15].

Here the shell thickness t_{sh} is deduced from chemical metal titrations, using the model of [7]. Table S1 collects the shell thickness values of the core@shell NPs used here, with a diameter $d_0^{TEM} \approx 9$ nm or less. The thickness of this layer is on average here ~ 0.5 nm, that is less than both the cell parameter of the core ferrite ($\sim 0.83 - 0.84$ nm) [9, 13] and of ideal maghemite (0.8356 nm).

Table S1: Shell thickness t_{sh} of core@shell NPs with $d_0^{TEM} \approx 9$ nm or less. t_{sh} is deduced from chemical titrations using the chemical core-shell model of Gomes et al [7]

NP	Core	d_0^{TEM} (nm)	t_{sh} (nm)
C1	$CoFe_2O_4$	8.6	0.53
D1	$CoFe_2O_4$	4.1	0.44
D2	$CoFe_2O_4$	8.9	0.35
E	$Cu_{0.15}Zn_{0.15}Co_{0.7}Fe_2O_4$	9.2	0.61

S1.2. Materials necessary for the various coatings of NPs

For the coating of the various NPs, tri-sodium citrate (Na_3Cit, Merck), N,N-Bis(trifluoromethanesulfonyl)imide acid (HTFSI, purity 95 %, Fluorochem); $HPAC_6MIM$ Br (1-methyl -3 -(hexyl phosphonic acid) imidazolium bromide) from Sikemia, France, are used as received.

$HPAC_6MIM$ TFSI is prepared from the commercial $HPAC_6MIM$ Br adding AgTFSI in a 1:1 ratio in water. The AgBr precipitate is removed by centrifugation and the supernatant is used as a solution with a concentration lower than 0.1 mol/L, which is close to the solubility of $HPAC_6MIM$ TFSI in water.

S1.3. Size sorting of the NPs in aqueous dispersions.

Dilute aqueous dispersions of magnetic nanoparticles (NPs) bearing also an electrostatic charge, they behave as « fluid dispersions » if the balance of interparticle interactions is repulsive. In the present case, the various interparticle interactions to which the NPs are submitted are the electrostatic repulsion due to the NP superficial charge, the van der Waals attraction and the magnetic dipolar interaction which is anisotropic (and attractive on average in zero magnetic field). The thermal agitation kT comes in balance with these interactions. When the isotropic interparticle attraction is strong enough (for example by increasing the ionic strength and thus the screening of the electrostatic repulsion), a liquid-liquid phase separation is observed [16]. It leads to a liquid concentrated phase co-existing with a very dilute liquid phase. The phase diagram is strongly dependent on the NPs size and it is possible to take advantage of this phase separation induced by the addition of salt to perform a size sorting of the NPs [4]. Here the size sorting is

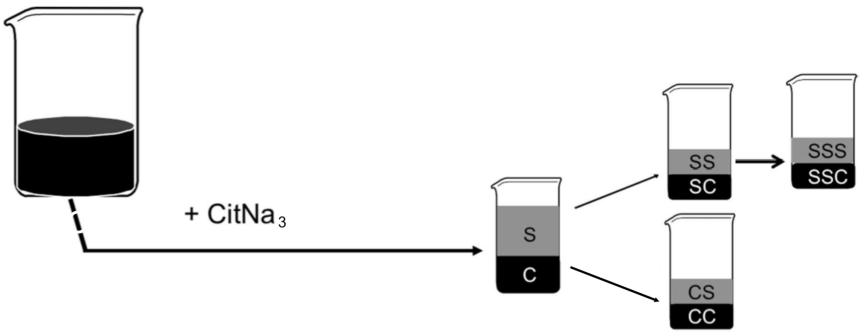

Figure S1: The addition of sodium citrate in the initial aqueous sample (dispersion of citrate-coated NPs) induces a phase separation in a dilute and a concentrated phase (respectively light grey and black in the figure). Further addition of sodium citrate in the isolated dilute and concentrated phases produces new phase separations. The operation is reproduced another time with the dilute phase issued from the first phase separation. As these phase separations are NP-size dependent, the distribution of NPs diameter issued by this process becomes thinner than the initial one.

performed on an aqueous dispersion based on citrate-coated C-NPs, which are core@shell $CoFe_2O_4$ @γ-Fe_2O_3 NPs, by progressive addition of sodium citrate following the scheme described in [4] and presented in Fig. S1. C1-NPs, C2-NPs and C3-NPs are respectively issued from dispersions SSS, SSC and CC. The black color of the dispersions of core@shell $CoFe_2O_4$ @γ-Fe_2O_3 NPs renders this operation difficult.

The same process is applied to obtain sample B, based on maghemite. Sample B is one of the fractions (SC type).

S1.4. Preparation and characterization of DES Reline : choline chloride-urea 1:2 (DES-ChU).

The following products are purchased and used as received: choline chloride (Sigma Aldrich) and urea (Sigma Aldrich). Table S2 shows the physical properties of choline Chloride and Urea. The water content is analyzed using coulometric Karl Fischer titration (Schott TitroLine KF Trace). The thermal gravimetric analyses (TGA) are performed using a TA Instruments SDT Q600 V20.9 Buid 20. The analyses are performed with a compressed air flow rate of 100.0 mL/mn and a temperature ramp that varied from 25 °C to 200 °C at 10 °C/mn.

The first Reline (DES-ChU) is produced by mixing of the two solids as received. Weighted amounts in the molar ratio Ch:U (1:2) are mixed and heated at 80 °C under stirring in a capped flask under N_2 atmosphere until a liquid is obtained [19]. Right after the obtention of DES-ChU the water content is about 0.27 w%, according to the Karl Fischer titration.

The second Reline (DES-ChU) is produced in the same way after drying the two solids separately during 24 hours in an oven at 80 °C before the mixing. The water content determined by the Karl-Fischer method is then 0.09 w%, therefore lower than in the first reline.

The liquid obtained is very viscous, with a melting point close to ambient temperature, around 27 °C, however supercooling is frequent, which enables measurements below the melting point, here down to 20 °C. To determine the melting point, the reline solvent with low water content has been subjected to a low heating. The obtained value is consistent with values found in the literature. Meng et al [20] observed that while heating the reline sample

Table S2: properties of the individual components of ChU at 25 °C

Properties	Choline chloride (ChCl)	Urea (U)
M (g/mol)	139.63	60.06
Melting T (°C)	247.00	132.70 [17]
ChCl Boiling T (°C)	decomposition	decomposition
Density (g/cm^3)	1.1000 [18] (for 70 w% in water)	1.3230 [17]
Molar vol. (cm^3/mol)	127±5 [18]	45.39 [17]

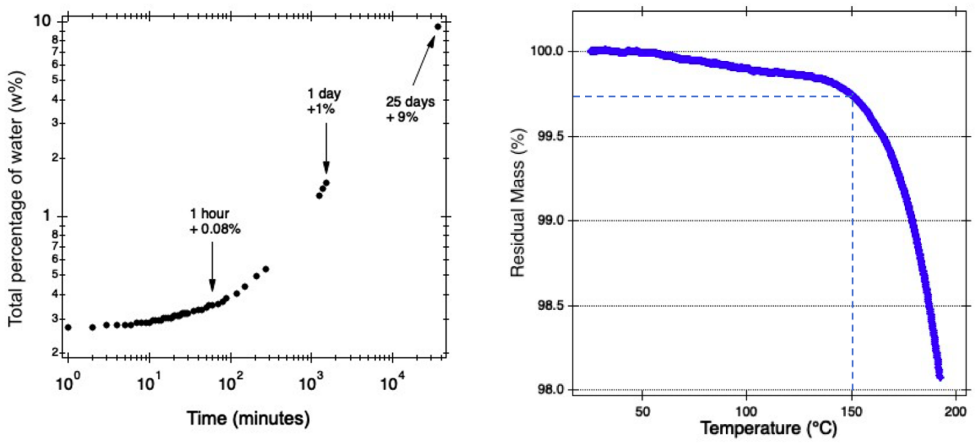

Figure S2: (Left) Total percentage of water in the DES as a function of the time from the opening of the bottle. Room temperature and atmospheric humidity (around 60%). The initial water content was 0.27w% at t=0.(Right) Thermogravimetric analysis of the DES - ChU (1:2) with a temperature ramp of 10.00 °C/mn from 25.00 °C to 200.00 °C under an air flow of 100 mL/mn. The initial amount of 0.27 w% water is lost at 150°C.

(1:2), a rapid transition from a white solid to a transparent liquid is observed between 30 and 35 °C and the eutectic temperature is proposed to be 25 °C for a water content lower than 2000 ppm (0.2 w%). Note that the use of hydrated components can produce a DES of molar composition different from the expected one, therefore changing the melting point [21]. Moreover, the melting point of eutectic mixtures decreases below room temperature when they absorb water from the atmosphere, which easily occurs due to their high hygroscopicity [20].

As contact with air is unavoidable at some step of the different measurements (Meng et al [20], over days), the water uptake of the first Reline (DES-ChU) in atmospheric conditions is measured with a focus on short times. For this purpose, a sample of around 12 g is left uncapped on a balance and is weighed regularly. The mass increase with time is shown on Fig. S2-left, which plots the total percentage of water. From the initial value of 0.27 w%, the increase is 0.08 w% after 1 hour and increases to 9 w% after 25 days. The DES is thus stored under nitrogen in closed bottles. This water increase is thus negligible in the first 10 minutes, meaning that our experiments are not affected by the very short times of contact with air at some steps, which have been less than 10 minutes in total.

Note that a water pollution in this Reline DES-ChU is very difficult to remove: freeze-drying, which pumps at low temperature, is extremely long and a high temperature would be necessary, above 80 °C, which is not compatible with the thermal stability of this DES, although it is one of the most stable due to the low volatility of urea and its thermal stability. This latter is difficult to precisely estimate for Reline and probably depends on the water content. In reference [22], Reline (DES-ChU) already loses around 1.52 w% after 20h at 70 °C in a DES with a water content lower than 0.5 w% but not precisely given. However, in the ramped experiment, Reline loses several percent of its mass at 150 °C in [22] although Fig. S2-right shows a loss of only 0.27%. The difference could be linked to a different water content between the two experiments and the long term stability could be higher for a lower water content.

These different results point towards the necessity to properly control the water content in the used Reline solvent and during the preparation of the colloidal dispersions, as this can strongly modify the properties. Therefore, all the colloidal dispersions have been done with the second Reline (DES-ChU) with 0.09 w% water, in the temperature range 20-45 °C, for which there is no doubt on the thermal stability of this solvent.

S1.5. Molecular structure of Reline (DES-ChU).

The local structure of Reline (DES-ChU 1:2)) has been studied by neutron diffraction and atomistic modelling by O.S. Hammond et al in [23]. It shows DES supramolecular structures linked together by strong hydrogen bonds preventing crystallization of the mixture at room temperature. Fig. S3 proposes a schematic representation of this Reline supramolecular structure, the mean distance choline-choline being $\sim$ 6.3 Å and the average coordination of choline being $\sim$ 7.

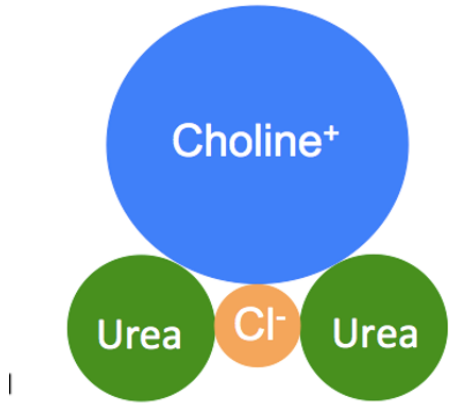

Figure S3: Schematic representation of the supramolecular structure of choline chloride /urea DES of composition 1:2 close to the eutectic point (Reline).

S1.6. Density and viscosity of mixture of water/Reline (DES-ChU) as a function of T.

A detailed study of density ρ and viscosity η of ChU containing controlled amounts of water, is performed in the temperature range 20-45 °C; Density ρ thanks to an Anton Paar DSA 5000M, with precision 10^{-6} g/mL and temperature accuracy < 10^{-3} °C; Viscosity η using an Anton Paar Automated MicroViscometer AMVn instrument by using the falling ball model in a 1.8 mm (resp. 3.0 mm) capillary with a 1.5 mm (resp 2.5 mm) falling ball. The instrument is first calibrated with reference standard oils N14 (resp. N44) from Cannon Instrument Company provided by Anton Paar (η =71.29 mPa.s (resp. 19.68 mPa.s), ρ = 0.8249 g/mL (resp. 0.8092 g/mL) at 25 °C)). Water is added in a DES containing initially 0.09 w% of water. The mixtures are done quickly by weighting and the vials are capped immediately. The viscometer capillary and the densimeter tube are filled as fast as possible and tightly capped before the measurements. Results are presented in Fig. S4.

Note that, although the water weight fractions are low and close to the volume fractions (5w% ≃ 6vol%), the conversion of these values in a microscopic description in number of molecules is quite different due to the small size of the water molecules. Assuming an ideal mixture, 1w% of water corresponds to 1 water for 6.8 ChCl:2urea and 5w% to 1 water for 1.3 ChCl:2urea.

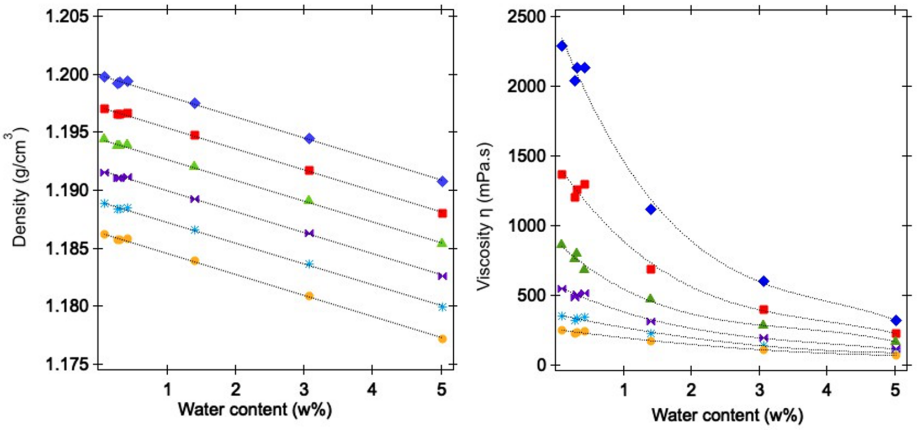

Figure S4: Density ρ (left) and viscosity η (right) of DES containing water vs water content (weight percent) for various temperatures. The water content takes into account the initial water content (0.09 w%) and the added amount. (Legend: 293.15 K: blue lozenges, 298.15 K: red squares, 303.15 K: green triangles, 308.15 K: purple double-triangles, 313.15 K: light blue star, 318.15 K: orange disk)

S1.7. NP transfer in the dense ionic fluids.

The NPs concentration is determined by flame atomic absorption spectroscopy in water. A volume of sample is dissolved in concentrated HCl, then diluted in 2w% HNO_3 and the concentrations of the different metals are determined using a calibration based on standard commercial solutions of the metals.

The first step for the NP transfer is the adaptation of the NPs'interface of the synthesized acidic samples. It is performed in pure water.

For alkaline samples in TMAOH or samples coated with the ligand PAC_6-MIM^+, the process is the one proposed by Riedl et al in Ref. [24] and further adopted by Guerra et al [11]. The PZC of the particles is first reached by addition of NaOH until pH=7 to remove their charge. This enables washing the initial nitrate counter-ions with ultrapure water because the NPs are floculated and easily sediment on a magnet. Once the remaining ion concentration is lower than 10^{-6} mol/L, the new species are added: TMAOH strong base to reach pH = 12 or $HPAC_6$-MIM^+ with bromide or TFSI anions with a total concentration of 0.075 mol/L, with a volume fraction of NPs of 1 vol%.

For samples with a sodium citrate coating, a solution at 0.025 mol/L citric acid is added to the initial acidic dispersion in nitric acid. The NPs floculate due to the adsorption of neutral citric molecules. They are washed with 0.025 mol/L citric acid solution until the concentration of nitrate is lower than 10^{-6} mol/L. A pH of 7.5 is then reached by addition of NaOH.

The second step for the NP transfer is the water removal.

For the ionic liquid EMIM TFSI, an equivalent volume of NPs in water and EMIM TFSI are mixed and stirred few minutes before pumping 24 h at a pressure between 0.0031 mbar and 0.02 mbar at room temperature.

For the DES, 24 h is not sufficient and around 66 hours are used at a pressure 0.013 mbar, to reach a low water level that cannot be directly measured by Karl Fischer technique because the solvent cannot be heated above 100°C.

Another way is used for the citrate coated NPs: the NPs are floculated with acetone added in water, then washed three times with acetone to remove water and once with ether at the end. The particles always stay in the solvent, never being dried, before addition of DES and heating at 60°C to remove the solvents before pumping as in the other route. Note that this process is not possible if the ligand is $HPAC_6$-MIM^+ Br^- because the NPs cannot be precipitated in water in the same way.

As already mentioned in section S1.6. for reline, a small weight percent of water corresponds to many molecules. For Reline 1w% water (1.2vol% water) corresponds to 1 H_2O for 6.8 ChCl:2urea. For EMIM TFSI, 1w% water (1.5vol% water) corresponds to 1 H_2O for 4.5 EMIM TFSI pair.

S2. Characterization techniques and Results

S2.1. Internal structure of core@shell NPs.

The influence of the maghemite shell on the crystallographic structure of core@shell NPs of different natures, synthesized with the present synthesis route, has been investigated in several works by x-ray powder diffraction and neutron powder diffraction - see for example [7, 13]. The internal crystalline structure is found continuous over the whole core and shell. The different chemical structure of the shell is evidenced in [14] by Scanning Transmission Electron Microscopy in the High Angle Annular Dark Field (STEM-HAADF) in Zn-Mn ferrites.

S2.2. Transmission Electron Microscopy of the NPs.

Shape and size distribution of the NPs are investigated by Transmission Electron Microscopy (TEM) images obtained at Sorbonne Université with a JEOL JEM-100 CX II microscope. In the micrograph images, the NPs appear as roughly spherical. The NP distribution of diameters is well accounted for by a log-normal law, given by:

$$P(d) = \frac{1}{\sigma d \sqrt{2\pi}} exp\left(-\frac{\ln^2(d/d_0)}{2\sigma^2}\right) \quad \text{(S1)}$$

allowing to deduce the median diameter (d_0^{TEM}) and the polydispersity (σ^{TEM}), as listed in Table 1 of main paper. An illustration is given in Fig S5 for NPs B, C1, C2 and C3.

Table S3: Ligands and counter-ions in EMIM-TFSI

Abbreviation	IUPAC Name	Molecular structure
Cit^{3-} $3Na^{+}$	Sodium Citrate	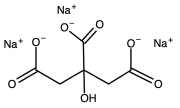
$HPAC_6MIM^{+}$ Br^{-}	1-methyl-3-(hexylphosphonic acid) imidazolium bromide	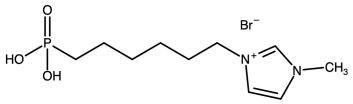
$HPAC_6MIM^{+}$ $TFSI^{-}$	1-methyl-3-(hexylphosphonic acid) imidazolium bis(trifluoromethanesulfonyl)imide	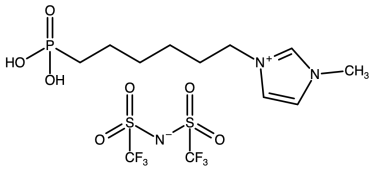

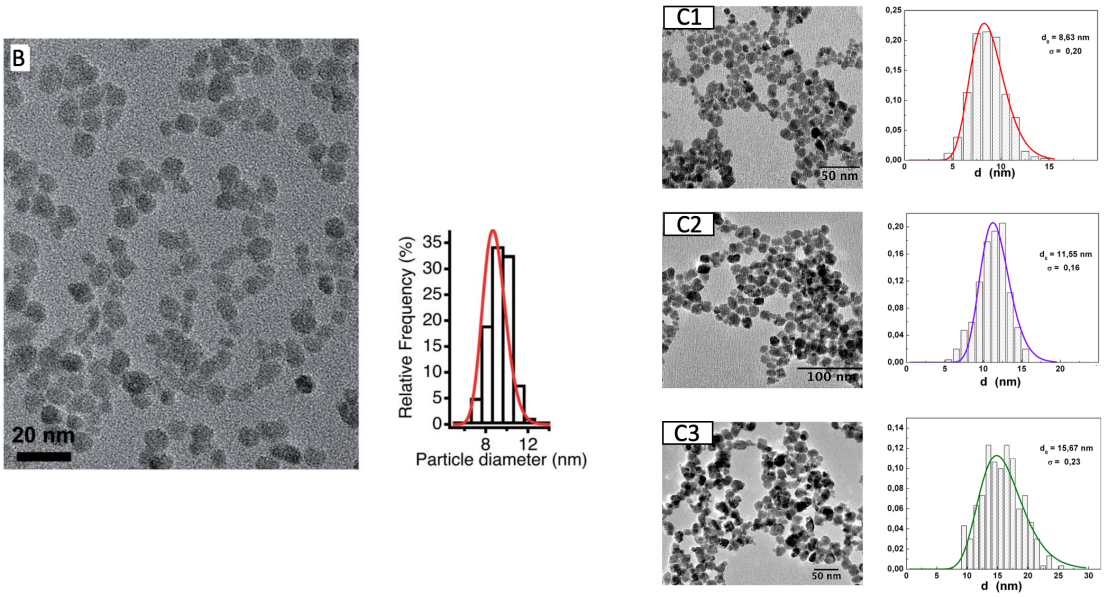

Figure S5: TEM images and their size distribution fitted with a log-normal distribution of diameter (left) maghemite B-NPs from Table 1 of main paper, (right) from top to bottom core@shell $CoFe_2O_4$ @γ-Fe_2O_3 C1-NPs, C2-NPs and C3-NPs.

S2.3. Homogeneity of the samples

Room temperature sample homogeneity is tested on the micron scale with an optical microscope (Olympus BX51 with lens 40x/0.6 and camera x5) in zero applied field. The stability under magnetic field is checked from the

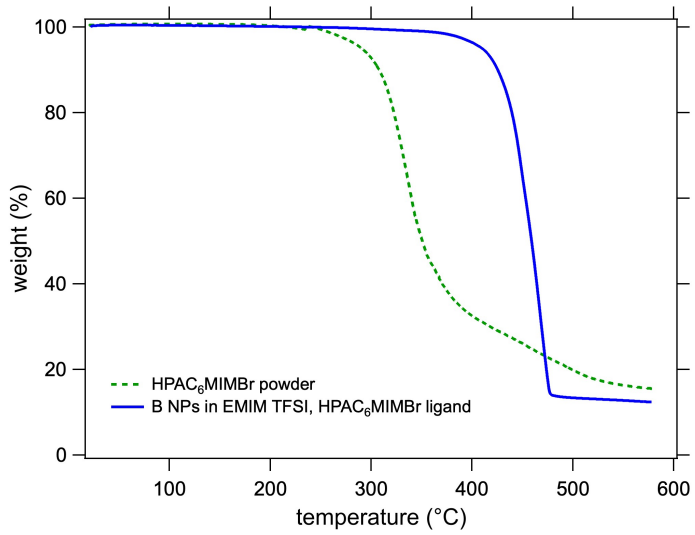

Figure S6: Ratio of the weight over the initial weight in % as a function of temperature while ramping up temperature at 10K / mn.

absence of diffraction pattern when the sample is illuminated by a He-Ne laser under the field of an electromagnet. Above the threshold of stability, a diffracted line appears in the direction perpendicular to the magnetic field due to the formation of needles or concentrated phase resulting from a phase separation [3, 16].

S2.4. TGA measurements

Thermogravimetric analysis (TGA) was performed with a TGA 550 from TA Instruments to evaluate the stability of samples in EMIM TFSI at the temperatures used for FRS measurements. 10 to 20 mg of sample is placed in an alumina crucible placed on a Pt crucible. The temperature is increased at 10 K/mn with a nitrogen flow of 50 ml/mn. Figure S6 shows the ligand PAC_6MIMBr and a dispersion of maghemite with this ligand in EMIM TFSI. It is the ligand that limits the stability of the dispersions above 200°C. The stability is maintained over the temperature range used here for the FRS measurements.

S2.5. Room temperature magnetization measurements

Magnetization (M) measurements of aqueous dispersions at NP volume fractions Φ of the order of 1% (or smaller) are performed at room temperature, as a function of the applied field H, either with a home-made vibrating sample magnetometer (VSM) up to 800 kA/m [25] in PHENIX - Paris or a Cryogenic S700X-R Superconducting Quantum Interference Device (SQUID) magnetometer, up to 5600 kA/m in Brasilia - Brazil. ***Analysis of the dispersion's magnetisation:*** Dispersions of superparamagnetic nanoparticles, monodisperse of diameter d, bearing a magnetic moment μ :

$$\mu = m_S \pi d^3/6 \tag{S2}$$

with of volume fraction Φ and a magnetic material magnetisation m_S have their magnetisation M ruled by the Langevin function $L(\xi)$ as a function of the applied field H:

$$M = m_S \Phi L(\xi) \tag{S3}$$

with

$$L(\xi) = \coth \xi - 1/\xi \tag{S4}$$

where ξ is the Langevin parameter:

$$\xi = \mu_0 \frac{\mu H}{kT}. \tag{S5}$$

If now the NPs are polydisperse in size, with a log-normal distribution of diameters $P(d)$:

$$P(d) = \frac{1}{\sigma d\sqrt{2\pi}} exp\left(-\frac{\ln^2(d/d_0)}{2\sigma^2}\right) \quad \text{with} \quad \int_0^{+\infty} P(d)\mathrm{d}d = 1, \tag{S6}$$

the magnetisation M of the dispersion can then be adjusted by:

$$\frac{M}{m_S\Phi} = \frac{\int_0^{+\infty} d^3 L\left(\xi(d)\right) P(d)\mathrm{d}d}{\int_0^{+\infty} d^3 P(d)\mathrm{d}d} \tag{S7}$$

as both μ and ξ are d-dependent:

$$\xi(d) = \mu_0 \frac{\mu(d)H}{kT}, \tag{S8}$$

as well as the volume fraction Φ which can be written as [25, 26]:

$$\Phi = \int_0^{+\infty} \Phi(d)P(d)\mathrm{d}d. \tag{S9}$$

where $\Phi(d)$ is the volume of a NP of diameter d times the total number of particle per unit volume. Note that in this analysis, the magnetisation m_S is supposed, in a first approximation, to be independent of the NP diameter.

At room temperature, for the analysis of the dispersion's magnetisation, the internal magnetic structure of the core@shell NPs is assimilated to a uniform structure. The individual magnetic contributions of the core and that of the shell are only important at very low temperatures.

To determine the magnetic characteristics (d_0^{magn}, σ^{magn} and m_S) of all the NPs used in this work, the experimental room-temperature magnetisation of their aqueous dispersions is fitted with the formalism of Eq. S7. These values are given in Table 1 of the main paper. See examples of such magnetisation curve in Fig. 1 of the main paper and in Fig.S7.

S2.6. Karl-Fischer (KF) method.

For the DES, KF titrations cannot be performed above 100°C, as the furnace requires heating the sample beyond this temperature for the measurement, which induces the decomposition of the DES, all the more so since the measurement typically lasts between 15 and 60 minutes. Colloidal dispersions nevertheless need to be measured with the furnace as it avoids false contributions due to the NPs and pollution of the whole solvent of the machine. Dispersions in the DES cannot therefore be studied.

With the furnace, the glass bottles with samples or background are prepared right before the titrations because there are long-term leaks. This enables measuring with a good reproducibility low amounts of water, with small

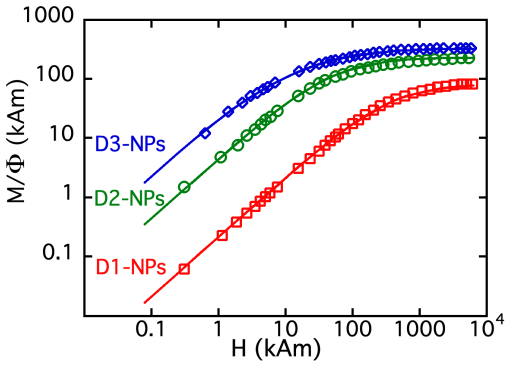

Figure S7: Log-log representation of the magnetisation as a function of applied magnetic field of core@shell $CoFe_2O_4$@γ-Fe_2O_3 D1-, D2- and D3-NPs from Table 1 of main paper, dispersed in water. Full lines are their fit with Eq. S7 and the parameters of Table 1 of main paper.

samples, typically 100 to 500 micrograms of water with a background around 10 micrograms.

S2.7. Small Angle X-ray Scattering (SAXS) measurements.

Room temperature small angle X-rays scattering (SAXS) experiments are carried out at the SWING beam line of Synchrotron Soleil (France) in a larger Q-range 2 10^{-3} Å^{-1} < Q < 2 10^{-1} Å^{-1}. The SAXS intensity $I(Q)$ is recorded at a beam energy chosen to limit x-ray absorption by iron in a flat glass capillary with a 100 μm thickness. Standard correction procedures are applied for sample volume, empty cell signal subtraction and detector efficiency to obtain the scattered intensity in absolute scale (cm^{-1}). Such data reduction is done using the software Foxtrot®. See examples of the SAXS scattered intensity I(Q) in Figs. 2 and 3 of the main paper and in Fig. S8 and S9.

The scattered intensity I(Q) is linked to the NP's structure factor $S(Q)$ and their form factor $F(Q)$ via the expression:

$$I(Q,\Phi) = (\Delta\rho)^2\ \Phi\ (\pi d_w^3/6)\ F(Q)\ S(Q,\Phi) \tag{S10}$$

where d_w is the NPs weight-average diameter (associated volume $V_w = \pi d_w^3/6$) and $(\Delta\rho)^2$ the contrast between the NPs and the solvent, which is given in Table S4.

At low Q's, the form factor $F(Q)$ of the NPs is given by:

$$F(Q) = e^{-\frac{1}{3}Q^2R_g^2} \quad \text{if} \quad QR_g \leq 1 \tag{S11}$$

and the structure factor $S(Q)$ of the NPs equals 1 at $\Phi = 0$.

The value of the structure factor at $Q = 0$ is a marker of the global interparticle interaction. If the interparticle interaction is globally attractive, $S(Q = 0, \Phi) \geq 1$ and $S(Q = 0, \Phi)$ gives the NP's aggregation number [27]. On the contrary, $S(Q = 0, \Phi) \leq 1$ if the interparticle interaction is repulsive. It then expresses as:

$$S(Q = 0, \Phi) = \left[\frac{\partial}{\partial\Phi}\left(\frac{\Pi(\Phi)V_W}{kT}\right)\right]^{-1} = \chi(\Phi) \tag{S12}$$

where $\Pi(\Phi)$ is the osmotic pressure and $\chi(\Phi)$ the isothermal compressibility of the NPs system.

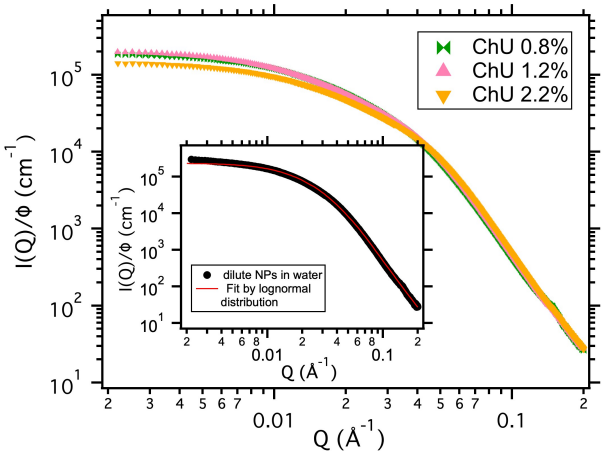

Figure S8: Small Angle X-Ray scattering intensities from the colloidal dispersions of A-NPs in ChU. Main graph: SAXS intensity normalized by the volume fraction for three volume fractions of NPs (see legend) in ChU after transfer from water. Inset: Intensity for the initial dispersion in water at $pH = 2$ for a very low concentration of NPs, and the fit by a lognormal distribution at $\Phi = 0.043$ vol% $d_0^{SAXS} = 5.2$ nm and $\sigma^{SAXS} = 0.5$.

Table S4: X-ray contrast between NPs and solvent

NPs / Solvent	Water	ChU - Reline	EMIM-TFSI
Maghemite	9.46 10^{22} cm^{-4}	8.54 10^{22} cm^{-4}	7.38 10^{22} cm^{-4}
Co ferrite	11.36 10^{22} cm^{-4}	10.35 10^{22} cm^{-4}	9.07 10^{22} cm^{-4}

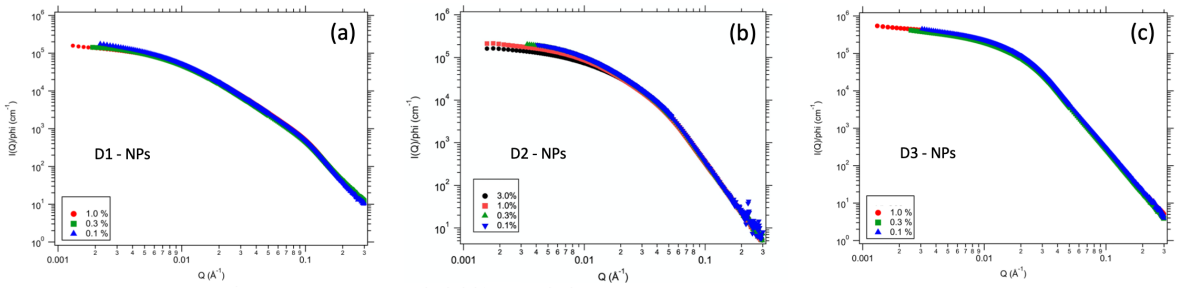

Figure S9: SAXS scattered intensity I(Q) normalized by the volume fraction of core@shell $CoFe_2O_4$ @γ-Fe_2O_3 (a) D1-NPs, (b) D2-NPs and (c) D3-NPs from Table 1 of main paper, dispersed in EMIM-TFSI.

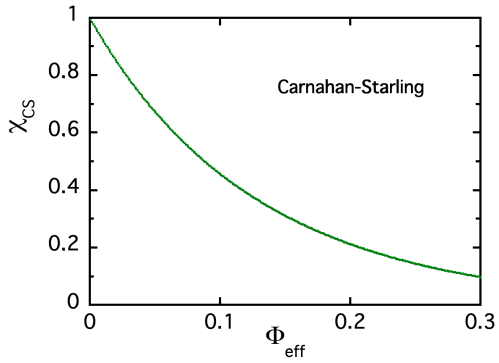

Figure S10: Carnahan-Starling compressibility χ_{CS} of effective hard spheres as a function of their volume fraction Φ_{eff}.

$\chi(\Phi)$ can be expressed here, as in [28] (see ESI therein), with the following hard-sphere Carnahan-Starling formalism χ_{CS}, with hard spheres of effective diameter $d_{NP} + 2l_s$ (where l_s is an effective screening length) and of effective volume fraction $\Phi_{eff} = \Phi(1 + 2l_s/d_{NP})^3$:

$$\chi_{CS}(\Phi_{eff}) = \frac{(1-\Phi_{eff})^4}{(1+4\Phi_{eff}+4\Phi_{eff}^2-4\Phi_{eff}^3+\Phi_{eff}^4)} \tag{S13}$$

Fig. S10 presents χ_{CS} as a function of the hard-shpere effective volume fraction Φ_{eff}. The second virial coefficient A_2 of the osmotic pressure Π in the dispersion can be obtained from the determination of Φ_{eff} with $\chi(\Phi) = \chi_{CS}(\Phi_{eff})$, without any hypotheses on the NPs size :

$$A_2 = A_2^{HS}\frac{\Phi_{eff}}{\Phi} \tag{S14}$$

where $A_2^{HS} = 4$. With an hypothesis on d_{NP} an evaluation of the effective screening length l_s can be produced if $A_2 \geq 4$.

Note that with a weakly repulsive interparticle interaction, $0 \leq A_2 \leq 4$ and with a weakly attractive interparticle interaction, $A_2 \leq 0$, Eq. S15 can be applied (with χ slightly larger than 1 for $A_2 \leq 0$) typically down to $A_2 \sim -5$ (see [29]). The values then obtained correspond to the more usual low Φ development of $\chi(\Phi)$:

$$\chi(\Phi) \approx \frac{1}{1+2A_2\Phi} \tag{S15}$$

S2.8. Dynamic Light Scattering (DLS) measurements

Dynamic light scattering (DLS) is performed at room temperature either with a Vasco instrument, operating at λ = 656 nm, or with a VascoKin DLS Particle Analyser, operating at λ = 638 nm, both from Cordouan technologies. Both instruments detect in backscattering (Vasco at θ = 135 ° and VascoKin at θ = 170 °), which avoids multiple scattering

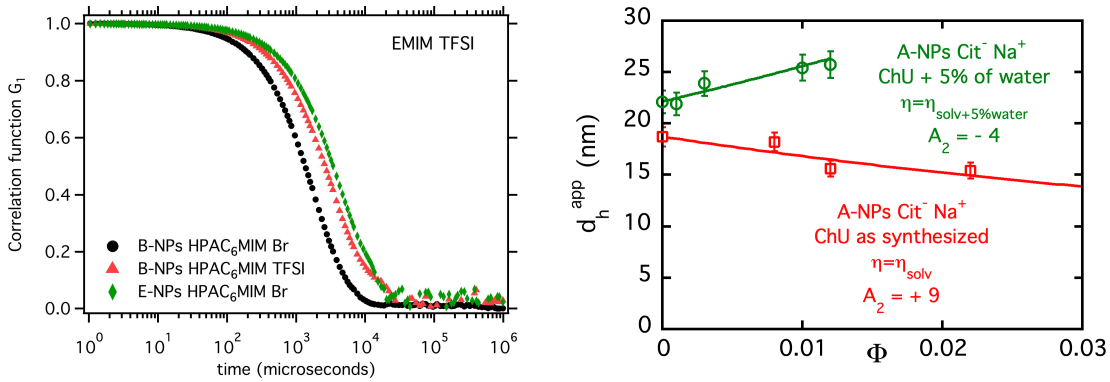

Figure S11: (left) DLS relaxation from the colloidal dispersions in EMIM-TFSI of B-NPs coated with $HPAC_6$-MIM^+ associated to either Br^- or $TFSI^-$ counterions and E(fresh)-NPs coated with $HPAC_6$-MIM^+ associated to Br^- counterions; (right) Apparent hydrodynamic radius d_h^{app} deduced from DLS at room temperature as a function of the volume fraction Φ for citrate-coated A-NPs dispersed in ChU, as synthesized (red squares) and in ChU + 5 vol% of water (green disks). In Eq. S17, the used viscosity is that of the synthesized solvent (ChU with +0.09vol% of water) for red squares and the measured viscosity of ChU + 5vol% of water for the green disks.

and allows measurements in optically absorbing samples such as ferrofluids with solvent index of refraction n_0. The measurement is done on a thin film in the Vasco (around 200 μm) and on a depth lower than 1 mm with the Vascokin. The corresponding scattering vector is $Q = \frac{4\pi}{\lambda} n_0 \sin(\theta/2)$, the solvent index of refraction n_0 being measured with a refractometer Arago from Cordouan Technologies at 656 nm.

The correlation functions (see examples in Fig. S11-left) are analysed with an analysis close to the cumulants proposed by B.J. Frisken in [30] to extract a diffusion coefficient D_m

$$D_m = \frac{kT}{\chi\zeta}. \tag{S16}$$

S2.9. Effect of NP-NP interaction on diffusion coefficient D_m - Extrapolation of the apparent hydrodynamic diameter d_h^{app} at $\Phi = 0$.

The diffusion coefficient D_m obtained by DLS as well as by FRS depends on the interparticle interaction though two terms, the compressibility χ and the friction ζ (see Eq. (2) of the main text and Eq. S16). A Φ-dependent apparent hydrodynamic diameter $d_h^{app}(\Phi)$ can be obtained in the following way:

$$D_m(\Phi) = \frac{kT}{3\pi\,\eta\, d_h^{app}(\Phi)} \quad \text{with} \quad d_h^{app}(\Phi) = \frac{\chi d_h}{(1 - 6.55\Phi)} \tag{S17}$$

Table S5: Evaluation of the interparticle interaction effect on the measured apparent hydrodynamic diameter at $\Phi = 1$ vol % (except (*) where it is evaluated at 2.5 vol%) using the A_2^{SAXS} values.

NPs	solvent	coating	counterions	A_2^{SAXS}	Φ_{eff}/Φ	$\chi(\Phi = 1\%)$	d_h/d_h^{app}
B	EMIM-TFSI	$HPAC_6$-MIM^+	Br^-	3.2	0.8	0.94	1,00
B	EMIM-TFSI	$HPAC_6$-MIM^+	$TFSI^-$	3	0.75	0.94	0.99
D2	EMIM-TFSI	$HPAC_6$-MIM^+	Br^-	4	1	0.923	1,01
E	EMIM-TFSI	$HPAC_6$-MIM^+	Br^-	0	0	1	0.836 (*)

where d_h is the hydrodynamic diameter at $\Phi = 0$. Fig. S11-right illustrates that for A-NPs dispersed in ChU with and without added water. In both cases, using Eq. S17, it is possible to deduce a value of the second virial coefficient of the osmotic pressure A_2 corresponding to a repulsion $A_2 = +9 \pm 2$ without added water and an attraction $A_2 = -4 \pm 1$ with 5vol% of added water (see the figure).

Table S5 compiles the values of the ratio d_h/d_h^{app} used in Table 4 of main text to deduce d_h (if direct extrapolation at $\Phi = 0$ from measurements at various Φ is not available) using A_2^{SAXS} values from Table 3 of main text.

S2.10. Small angle neutron scattering (SANS) probing of PAC_6-MIM^+ coated B-NPs with Br^- counter-ions as a function of T

The SANS experiments from [31], were performed at PAXY, LLB – Saclay – France, as in [24]. A furnace was fixed on a controlled rotating table to ensure a reproducible position for all samples. The oven was filled with nitrogen gas to work under inert atmosphere. As only classical circular quartz/spacer/quartz sandwich could fit in this furnace and no change of the furnace was possible, adapted cells were developed, making it possible to heat liquid samples in the furnace. The cells are based on a Teflon spacer glued on quartz with a hole on the top to evacuate gases that may escape during the heating process (the cell is left open). The data presented come from neutron runs which combined three configuration λ = 5 Å, d=1m; λ = 5 Å, d=3 m and λ = 8.5 Å, d=5 m. Figure S12 presents the SANS scattered intensity of dispersions in EMIM TFSI of B-NPs with PAC_6-MIM^+ coating and Br^- counter-ions at various temperatures from 300 K up to 473 K, and back at 300 K, without sensitive variation, confirming the thermal stability of the sample and the independence of the interparticle interaction in the experimental range of Φ and T.

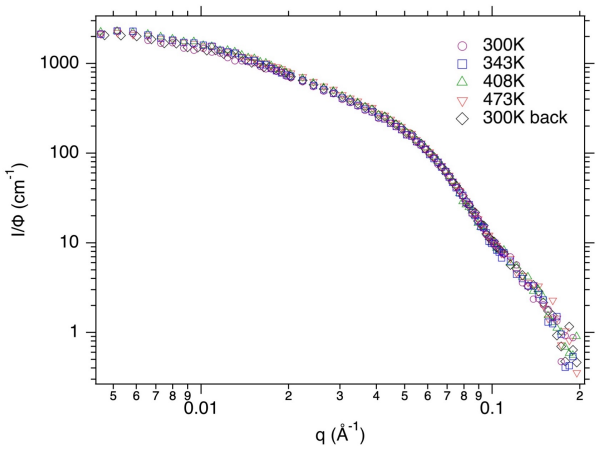

Figure S12: SANS absolute scattered intensities (normalised by the nanoparticle volume fraction Φ = 0.85 vol%) of B-NPs dispersions with PAC_6-MIM^+ coating and Br^- counterion in EMIM TFSI, at different temperatures (300 K (circles), 343 K (squares), 408 K (up triangles), and 473 K (down triangles) and back at 300 K (losanges)) as a function of the scattering vector Q.

S2.11. Thermodiffusion measurements

Thermodiffusive and thermophoretic properties are here probed with a home-made Forced Rayleigh Scattering (FRS) device, described in details in [32, 33, 34] and in ESI of [28].

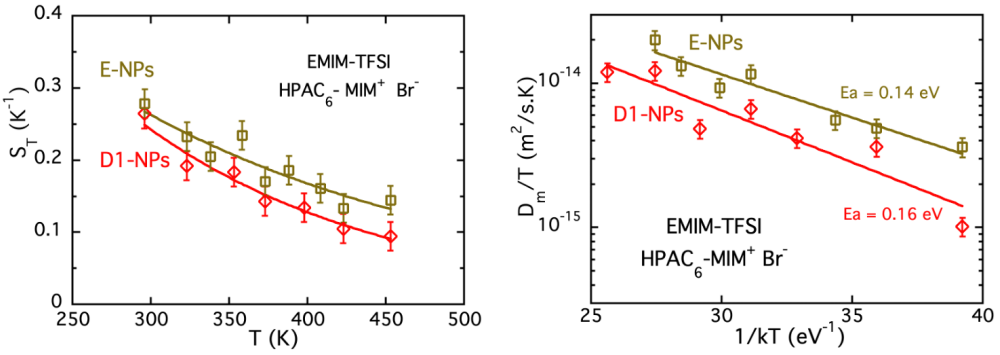

Figure S13: FRS of recently prepared (and un-heated) samples in EMIM-TFSI based on D1-NPs and E-NPs. Measurements for D1-NPs are performed at Φ = 1 vol% and for E-NPs at Φ = 2.5 vol%.

Briefly, the NP liquid-dispersions are sealed in flat glass cells (25 μm-thick). A high-power white lamp, temporally modulated at 4Hz or 8Hz, produces the image of a grid, inside the optical cell, with a spatial modulation ~ 100 μm. Temperature gradients are induced in the sample with the same modulations, because of the large NP absorption in the visible spectrum. Thanks to the Ludwig-Soret effect [35, 36], the temperature gradients $\vec{\nabla}T$ induce NPs concentration gradients $\vec{\nabla}\Phi$ in the dispersion. The diffraction of a non-absorbing He-Ne laser beam probes the associated optical-index modulations. The optical-index contributions due to volume fraction inhomogeneities (always seen when the power lamp is on and off) are 10^3 slower than the contributions due to temperature inhomogeneities (only seen when light is on). They can thus be easily separated. The Soret coefficient S_T is defined, in the stationary state, by:

$$\vec{\nabla}\Phi = -\Phi S_T \vec{\nabla}T \tag{S18}$$

The translation diffusion coefficient D_m is determined by the diffraction relaxation of the probing He-Ne laser beam, when the high-power lamp is switched off. The temperature gradients relaxing very quickly, the long-time relaxation corresponds to the displacement of the NPs to recover a random homogeneous distribution. The relaxation is analysed as a simple exponential process.

Figure S13 presents temperature variations of S_T and D_m/T for the samples based on recently prepared NPs-D1 and NPs-E dispersed in EMIM-TFSI with a $HPAC_6$-MIM^+ coating and Br^- counterions.

S2.12. Ultracentrifugation

Dispersions based on the ionic liquids EMIM-TFSI can be separated into a dense phase and a supernatant by ultracentrifugation. The samples are sealed in quickseal tubes of 2 ml. An Optima 70 Ultracentrifuge from Beckman Coulter is used with a 100 Ti rotor rotating at 50000 rpm during around 42 hours. At the end, a clear supernatant can be extracted (see Figure S14). It enables titrating the water in the solvent around the NPs.

Figure S14: Tubes of the dispersion in EMIM TFSI after 42 h of ultracentrifugation at 50000 rpm.

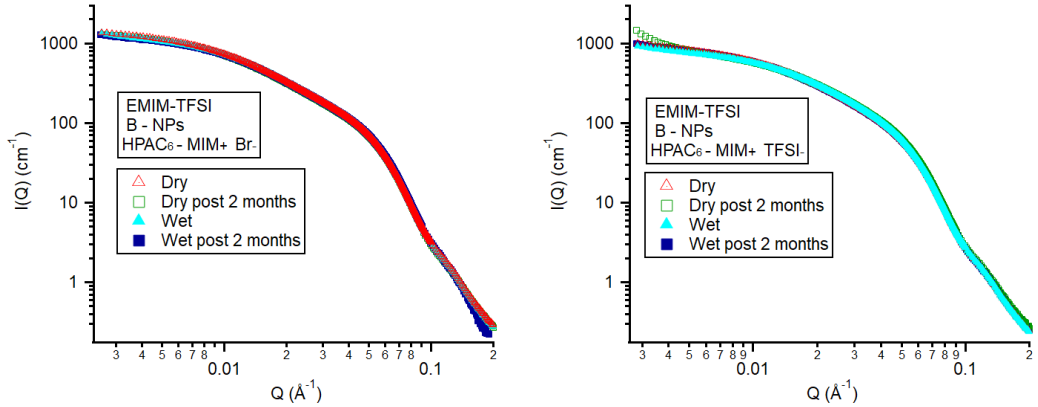

Figure S15: Small Angle X-Ray scattering intensities from the colloidal dispersions of B-NPs in EMIM-TFSI coated with $HPAC_6$-MIM^+ and Br^- counterions (left) and $HPAC_6$-MIM^+ and $TFSI^-$ counterions (right). The volume fraction is close to 1%. Empty symbols correspond to the samples obtained by the classical process (the driest ones, called dry) while full ones correspond to wet samples, that stayed 72 hours in a humid atmosphere. Triangle symbols correspond to the initial samples, and square ones to the same samples after two months.

S2.13. Nanostructure of wet samples with SAXS

Although EMIM-TFSI is hydrophobic, it can dissolve up to 1-2 vol% of water according to our results, a value similar to these found in literature, which are quite dispersed between the different studies. Our conclusion is that it depends on the hydration process. Here the samples are not saturated, they have been hydrated in the same conditions in the same glassware during the same time with two different counterions so that they can be compared. With $HPAC_6$-MIM^+ coating and Br^- counterions, water increases up to 0.52 vol% while it increases only up to 0.22 vol% with $HPAC_6$-MIM^+ and $TFSI^-$.

The SAXS measurements (Figure S15) evidence no visible influence of hydration on the structure, which means that hydration changes neither the interparticle interaction nor the aggregation. The only change occurs in the dry sample with $HPAC_6$-MIM^+ coating and $TFSI^-$ counterions after 2 months, showing a small upturn at low scattering vectors, which can correspond to the formation of small aggregates. This could change the hydrodynamic diameter, however its determination would necessitate the viscosity, which depends on the water amount in the solvent, not a priori known.

References

[1] R. Massart, *I. E. E. E. Trans. Mag.*, 1981, **MAG-17**, 1247.

[2] J. Jolivet, R. Massart and R. Fruchart, *Nouv. J. Chim.*, 1983, **7**, 325–331.

[3] J. Bacri, R. Perzynski, D. Salin, V. Cabuil and R. Massart, *J. Magn. Magn. Mat.*, 1990, **85**, 27–32.

[4] R. Massart, E. Dubois, V. Cabuil and E. Hasmonay, *J. Magn. Magn. Mat.*, 1995, **149**, 1–5.

[5] S. Lefebure, E. Dubois, V. Cabuil, S. Neveu and R. Massart, *J. Mat. Research*, 1998, **13**, 2975–2981.

[6] F. Tourinho, R. Franck and R. Massart, *J. of Materials Science*, 1990, **79**, 3249–3254.

[7] J. Gomes, M. Sousa, F. A. Tourinho, R. Aquino, G. J. da Silva, J. Depeyrot, E. Dubois and R. Perzynski, *J. Phys Chem. C*, 2008, **112**, 6220–6227.

[8] R. Aquino, F. Tourinho, R. Itri, M. e Lara and J. Depeyrot, *J. Magn. Magn. Mat.*, 2002, **252**, 23–25.

[9] A. Moreira, F. Paula, A. Campos and J. Depeyrot, *Journal of Solid State Chemistry*, 2020, **286**, 121269.

[10] A. Campos, R. Aquino, F. Tourinho, F. Paula and J. Depeyrot, *Eur. Phys. J. E*, 2013, **36**, 42.

[11] A. A. A. M. Guerra, G. Gomide, S. Ibrahim, P. Burckel, P. Coppola, J. Depeyrot, R. Perzynski, V. Peyre, S. Papovi'c, M. Vranes, E. Dubois and A. F. C. Campos, *Colloids and Surfaces A: Physicochemical and Engineering Aspects*, 2024, **703**, 135233 1–10.

[12] B. Pereira, *Doctoral Thesis, University of Brasilia, Brazil*, 2025.

[13] F. H. Martins, F. L. O. Paula, R. C. Gomes, J. A. Gomes, R. Aquino, F. Porcher, R. Perzynski and J. Depeyrot, *Braz. J. Phys.*, 2021, **51**, 47–59.

[14] V. Pilati, R. C. Gomes, G. Gomide, P. Coppola, F. G. Silva, F. L. Paula, R. Perzynski, G. F. Goya, R. Aquino and J. Depeyrot, *J. Phys. Chem. C*, 2018, **122**, 3028–3038.

[15] R. C. Gomes, V. Pilati, F. H. Martins, F. G. da Silva, G. Gomide, B. C. C. Pereira, P. Coppola, F. L. de Oliveira Paula, A. F. C. Campos, C. Kern, G. F. Goya, F. Porcher, R. Aquino, E. Dubois, R. Perzynski and J. Depeyrot, *Nanoscale*, 2026, **18**, 10711–10723.

[16] F. Cousin, E. Dubois and V. Cabuil, *Phys. Rev. E*, 2003, **68**, 021405 1–9.

[17] *Handbook of Physics and Chemistry - 78rdEd.CRC press - Boca Raton*, 1997, **-**, –.

[18] *Chemical Safety Information from Intergovernmental Organizations Choline Chloride, Tech. Rep. OECD Screening Information Data Set 2004*, 2004, **-**, –.

[19] E. Durand, J. Lecomte and P. Villeneuve, *Eur. J. Lipid Sci. Technol.*, 2013, **115**, 379–385.

[20] X. Meng, K. B.-B. P. Husson and J.-M. Andanson, *New J. Chem.*, 2016, **40**, 4492–4499.

[21] T. E. Achkar, S. Fourmentin and H. Greige-Gerges, *J. Mol. Liq.*, 2019, **288**, 111028.

[22] N. Delgado-Mellado, M. Larriba, P. Navarro, V. Rigual, M. Ayuso, J. García and F. Rodríguez, *J. Mol. Liq.*, 2018, **260**, 37–43.

[23] O. Hammond, D. Bowron and K. Edler, *Green Chem.*, 2016, **18**, 2736–2744.

[24] J. Riedl, M. Sarkar, T. Fiuza, F. Cousin, J. Depeyrot, E. Dubois, G. Mériguet, R. Perzynski and V. Peyre, *J. Colloid Interface Sci.*, 2022, **607**, 584–594.

[25] J. Bacri, R. Perzynski, D. Salin, V. Cabuil and R. Massart, *J. Magn. Magn. Magn. Mat.*, 1986, **62**, 36–46.

[26] J. Bacri, R. Perzynski, D. Salin and J. Servais, *J. Physique*, 1987, **48**, 1385–1391.

[27] B. Frka-Petesic, E. Dubois, V. Dupuis, F. Cousin and R. Perzynski, *Magnetohydrodyn.*, 2013, **49**, 328–338.

[28] T. Fiuza, M. Sarkar, J. C. Riedl, M. Beaughon, B. Torres-Bautista, K. Bhattacharya, F. Cousin, E. Barruet, G. Demouchy, J. Depeyrot, E. Dubois, F. Gelebart, V. Geertsen, G. Meriguet, L. Michot, S. Nakamae, R. Perzynski and V. Peyre, *Phys. Chem. Chem. Phys.*, 2023, **25**, 28911–28924.

[29] T. Fiuza, M. Sarkar, J. Riedl, F. Cousin, G. Demouchy, J. Depeyrot, E. Dubois, R. Perzynski and V. Peyre, *Faraday Disc.*, 2024, **253**, 441–457.

[30] B. J. Frisken, *App. Opt.*, 2001, **40**, 4087–4091.

[31] J. Riedl, *Doctoral Thesis, Sorbonne Université - Paris, France*, 2020.

[32] G. Demouchy, A. Mezulis, A. Bée, D. Talbot, J. Bacri and A. Bourdon, *J. Phys. D: Appl. Phys*, 2004, **37**, 1417–1428.

[33] M. Sarkar, J. Riedl, G. Demouchy, F. Gelebart, G. Meriguet, V. Peyre, E. Dubois and R. Perzynski, *Eur. Phys. J. E*, 2019, **42**, 72 1–10.

[34] T. Fiuza, M. Sarkar, J. Riedl, A. Cebers, F. Cousin, G. Demouchy, J. Depeyrot, E. Dubois, F. Gelebart, G. Meriguet, R. Perzynski and V. Peyre, *Soft Matter*, 2021, **17**, 74566–4577.

[35] C. Ludwig, *Sitzungsber. Akad. Wiss. Wien, Math.-Naturwiss. Kl., Abt. 2A*, 1856, **20**, 539.

[36] C. Soret, *C. R. Arch. Sci. Phys. Nat., Arch. Genève IIIeme période,1879, 2, 48 - J. Phys. Theor. Appl.,*, 1880, **9**, 331–332.